International Journal of Heat and Mass Transfer 60 (2013) 163–169

Contents lists available at SciVerse ScienceDirect

International Journal of Heat and Mass Transfer

journal homepage: www.elsevier.com/locate/ijhmt

Planar vapor chamber with hybrid evaporator wicks for the thermal management of high-heat-flux and high-power optoelectronic devices

Y. Sungtaek Ju [a,*], M. Kaviany [b], Y. Nam [a,c], S. Sharratt [a], G.S. Hwang [b], I. Catton [a], E. Fleming [d], P. Dussinger [d]

[a] University of California, Los Angeles, CA, USA
[b] University of Michigan, Ann Arbor, MI, USA
[c] Kyung Hee University, Yongin, Republic of Korea
[d] Advanced Cooling Technologies Inc., PA, USA

ARTICLE INFO

Article history:
Received 17 July 2012
Received in revised form 30 November 2012
Accepted 27 December 2012

Keywords:
Vapor chamber
Heat pipe
Evaporator
Wick
Phase change heat transfer

ABSTRACT

Heat spreaders based on compact vapor chambers offer one attractive approach to the thermal management of high-power electronics. We report our design and experimental characterization of advanced evaporator wicks and thin planar vapor chambers incorporating these wicks. The hybrid wicks combine distributed high-permeability liquid supply structures with thin (monolayer) evaporation layers to achieve both low thermal resistance and high limiting heat fluxes over large heating areas. We model and experimentally characterize the capillary and heat transfer performance of liquid spreading layers consisting of mono-layers of Cu particles and identify a range of optimal particle diameters maximizing their performance. The thin liquid spreading layers are integrated with three different types of liquid supply structures, namely, columnar arteries, converging lateral arteries, and bi-porous structures. The resulting hybrid wicks show comparable heat transfer performances with critical limiting heat fluxes >350 W/cm^2 over heating areas of 1 cm^2 and peak heat transfer coefficients >20 W/cm^2 K. These results confirm the effectiveness of our hybrid wick designs and also that evaporation heat transfer is dominated by the liquid spreading layers. A prototype vapor chamber incorporating CTE-tailored envelopes and the hybrid wick is developed for potential applications in the thermal management of laser diode arrays. We demonstrate an evaporator resistance of approximately 0.075 K/(W/cm^2), while removing over 1500 W from a 4 cm^2 heating area.

1. Introduction

Advanced high-power and high-power-density electronic and optoelectronic devices very often require innovative thermal management solutions to ensure their reliable operations. One attractive approach is to passively spread the thermal energy over a large area using a thin planar vapor chamber before it reaches a downstream heat sink. This helps circumvent various reliability challenges of high-performance cooling solutions based on microchannels, such as corrosion or erosion of channel walls, pump failures, and various modes of flow instabilities (for two-phase flow cooling).

The thermal resistance of vapor chambers is most often dominated by that of the evaporators. Thin evaporator wicks with high effective thermal conductivity are desired to reduce the evaporator thermal resistance. Such thin wicks, however, suffer from low critical limiting heat fluxes due to their large liquid hydraulic resistances. These two conflicting considerations present significant challenges in designing effective evaporator wicks for handling large arrays of high-heat flux devices, such as laser diodes and RF/MW amplifiers.

Previous studies reported various wick structures developed for thin vapor chambers [1–4]. These past wick designs, however, were limited to small heating regions ($\ll$1 cm^2) or relatively low heat fluxes (<100 W/cm^2).

We report our efforts in developing hybrid wick structures where we integrate a thin liquid spreading layer with separate liquid supply structures to achieve an optimal balance between a small wick thermal resistance and a high critical limiting heat flux. Our previous work [5,6] discussed modeling of the liquid supply structures for one fixed liquid spreading layer design. We discuss here our efforts to optimize the capillary and heat transfer performance of monolayers of sintered Cu particles for use as liquid spreading layers. Heat transfer performance of various hybrid wicks that integrate the optimized liquid spreading layers with different types of liquid supply structures is next compared.

Vapor chambers for electronics cooling have typically been manufactured using copper or aluminum, which require compliant

* Corresponding author. Address: 420 Westwood Plaza, Los Angeles, CA 90095-1597, USA. Tel.: +1 310 825 0985; fax: +1 310 206 2302.
E-mail address: just@seas.ucla.edu (Y.S. Ju).

0017-9310/$ - see front matter
http://dx.doi.org/10.1016/j.ijheatmasstransfer.2012.12.058

interface materials like thermal greases and pads to accommodate mismatch in the coefficient of thermal expansion with electronic or optoelectronic devices. As device heat flux increases, most existing thermal interface materials are no longer effective due to their relatively low thermal conductivity. Direct chip bonding is far superior from a thermal resistance point of view but is more prone to failures by thermomechanical stress. We also report the design, fabrication, and experimental characterization of a prototype planar vapor chamber incorporating our hybrid wick on envelopes whose coefficient of thermal expansion (CTE) has been tailored to closely match laser diodes.

2. Hybrid wick designs

The basic design philosophy of our hybrid evaporator wicks is to separate the liquid supply function from the heat transfer function. Fig. 1 schematically illustrates three types of hybrid wicks that incorporate different liquid supply structures: (a) an array of vertical columnar arteries [5], (b) converging lateral finger-like arteries [6], and (c) a bi-porous structure of sintered particles [7].

The thin liquid spreading layer can be either a monolayer of sintered metal particles or an array of microfabricated posts with high effective thermal conductivity. Its thinness enables us to achieve very high evaporator heat transfer coefficient. The liquid supply structure sits on top of the liquid spreading layer to deliver liquid at *multiple* spots over an evaporator surface. This distributed liquid delivery scheme enables the liquid to spread efficiently along the spreading layer and keep a large evaporator surface wetted even at very high heat fluxes. The vapor generated through evaporation of the liquid layer readily escapes through large "pores" (space between arteries or particle clusters), reducing pressure drop for vapor flows.

3. Modeling and characterization of liquid spreading layers

Our previous publications reported detailed modeling and experimental studies of one type of thin liquid spreading layers: arrays of microfabricated Cu posts of heights of the order of 100 μm [8,9]. The geometric parameters of such micro-posts are precisely defined, facilitating the validation of theoretical models for their capillary and heat transfer performance.

An alternative option is monolayers of sintered metal particles. These monolayers can be fabricated using the same manufacturing processes as conventional wicks and therefore be more readily integrated with our liquid supply structures. We therefore focus on these monolayers of metal particles in this study.

Many previous studies reported heat transfer characteristics of sintered Cu particles but mostly for much thicker layers [10,11]. Visualization and modeling studies of the meniscus of well-wetting evaporating liquids around large macro-scale copper spheres were also reported [12]. We expand upon this and other work by developing models for their capillary and heat transfer performance and comparing their predictions with experimental results.

3.1. Sample preparation

In the present work, monolayer samples were prepared using a process analogous to self-assembly of particles. We first sieve Cu particles, suspend them in a solvent, and coat the resulting solvent–powder mixture on a 500 μm-thick Cu substrate (3 × 3 cm area). As the solvent is dried off, the particles aggregate and assemble on the substrate. The samples are then sintered in a hydrogen furnace for 1 h at 960 °C.

Samples made of particles of three different average diameters were studied: 29, 59, and 71 μm. Fig. 2 shows representative SEM images of these samples. The average powder diameter and distribution are determined by analyzing SEM images at multiple locations across the sample surfaces and listed in Table 1. The standard deviation in the powder diameter was as high as ±30% for the smallest particles due to limitations of our mechanical sieving process.

3.2. Modeling

The shape of a liquid meniscus around each Cu powder is a key factor that influences the capillary and heat transfer performance. To help validate, albeit indirectly, our experimental results and gain further physical insight, we construct approximate numerical models. We first employ the surface energy minimization algorithm to predict the "*static*" shape of a liquid meniscus for a "fictitious" unit cell consisting of a group of four spherical particles obtained from SEM images (see Fig. 3). "Random" spatial variations in the powder diameter and the relative powder location over each sample were not taken into account in this very approximate model.

Modeling the so-called thin film/interline region presents significant computational challenges. We consider an "apparent" contact as an adjustable parameter to approximately represent the impacts of evaporation and interfacial forces on thin evaporating liquid films and predict the heat transfer coefficient as a function of this parameter. A similar approach was adopted in our recent studies [8,9,13].

The particle–substrate contact is also important for both heat transfer (point contact of a spherical particle to the substrate

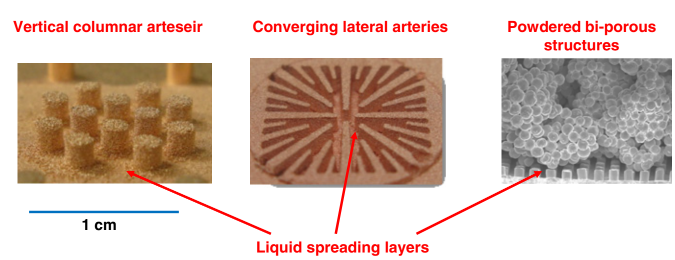

Fig. 1. Three different hybrid wicks considered in the present study with different types of liquid supply structures: vertical columnar arteries (side view), converging lateral arteries (top view), and bi-porous structures (side view).

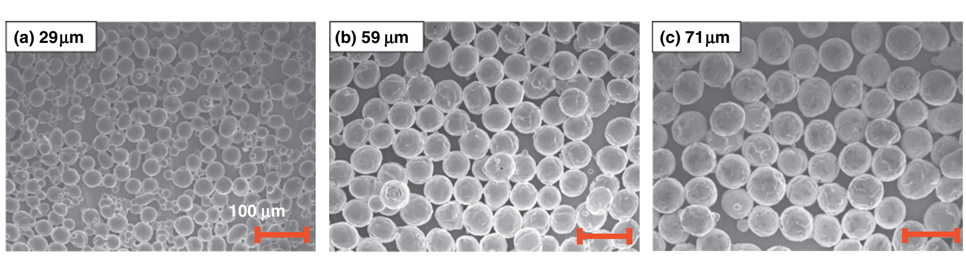

Fig. 2. SEM images of monolayers of sintered Cu particles of different average diameters: (a) 29 μm, (b) 59 μm, and (c) 71 μm.

Table 1
Geometric properties of the monolayers of sintered Cu particles.

Average diameter (μm)	Standard deviation (μm)	Solid fraction (%)
29	8	35
59	6	38
71	5	37

would add significant thermal resistance) and capillary pressure. Based on SEM images, we model Cu particles as truncated spheres with a ratio between the neck radius and the particle radius of 0.3.

The capillary pressure is computed from the surface curvature of a predicted meniscus profile for different values of the apparent contact angle and the liquid fill factor. The liquid fill factor serves as a relative measure of the liquid volume and is defined as the relative (with respect to the particle) height a liquid layer of a given volume would have if its meniscus were flat.

Representative images of the simulated static menisci are shown in Fig. 3 for different values of the liquid fill factor. Water is used as the working fluid for all results presented here. The predicted "static" meniscus shapes were imported into finite element liquid flow models (to predict the permeability, K) and heat transfer models (to predict the effective heat transfer coefficient, h_{eff}).

For the liquid flow model, the no-slip boundary condition is applied on all the particle and wall surfaces. The symmetry condition is applied on the side walls of the unit cell. The shear-free boundary condition is applied on the liquid meniscus. A periodic boundary condition is applied at the inlet and outlet of the unit cell. The heat transfer model accounts for solid and liquid heat conduction and evaporation at the liquid meniscus surface. Only pure conduction is considered in the heat transfer model as a previous study suggested that the internal convection has relatively small effects [14,15]. Further details of the models are provided in [8,9,13].

A grid independence study was performed to verify simulation accuracy. Increasing the number of surface mesh elements by 33% resulted in <1% change in h_{eff}. Doubling the number of volume mesh elements in the thin film region also resulted in less than <1% change in h_{eff}.

The predicted capillary pressures for a sample with particles of average diameter 59 μm are shown in Fig. 4. The calculated capillary pressure first increases with the increasing liquid fill factor and reaches a peak at a liquid fill factor approximately 0.5. This liquid fill factor value is assumed to correspond to a quasi-equilibrium location of liquid meniscus. The capillary pressure decreases with further increase in the liquid fill factor once smallest gaps between neighboring particles become submerged below the liquid meniscus.

Previous studies [16] experimentally demonstrated that the capillary pressure of bulk sintered powder plugs is primarily a function of the particle diameter. The predicted peak capillary pressure of the monolayers is comparable to the previous results obtained from bulk sintered powder plugs of similar particle diameters.

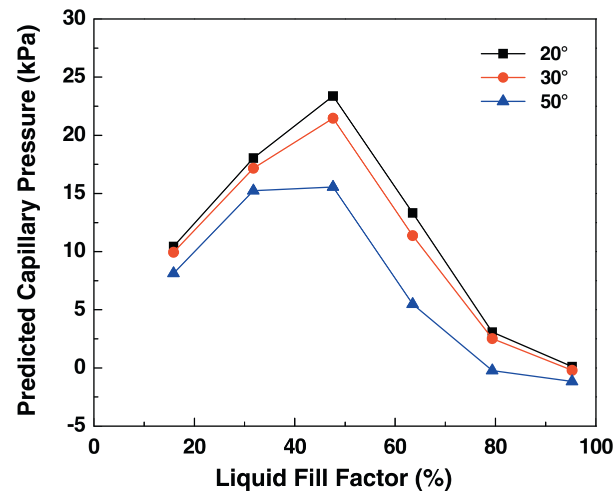

Fig. 4. Predicted capillary pressure of a monolayer powder sample as a function of the liquid fill factor for different values of the apparent contact angle.

The permeability is also calculated for different values of the apparent contact angle as a function of the liquid fill factor (Fig. 5). The apparent contact angle has a small overall effect on the permeability. The apparent contact angle affects permeability through changes in the shape of the liquid meniscus. At a given liquid fill factor, smaller apparent contact angles lead to skinnier menisci on particle surfaces (larger flow resistance) but higher overall meniscus heights (smaller flow resistance). The two factors offset each other, resulting in weak dependence of the permeability on the apparent contact angle.

3.3. Experiments

We performed capillary rate of rise experiments to determine the capillary performance parameter, which is defined as the ratio between the liquid permeability K and the effective pore radius R_{eff}, of the monolayers. This parameter compares the driving force (capillary force) for liquid flows along a liquid spreading layer against the hydraulic resistance. It is therefore a key determinant of the capillary limit of the layer. Details of the capillary rate of rise experiments are discussed in our earlier publication [8]. Briefly, we orient a dry sample vertically and bring its tip into contact with a liquid reservoir below. We optically monitor the location of the

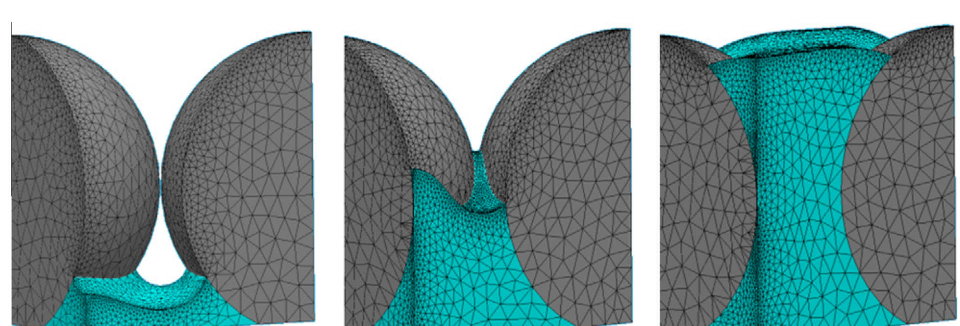

Fig. 3. Representative images of the simulated static menisci for different values of the liquid fill factor.

advancing meniscus front as a function of time. The time trajectory is then analyzed to determine the parameter K/R_{eff} that best fits the capillary rise data.

The heat transfer performance of the monolayers was characterized using a thermosyphon-like experimental setup reported earlier [9]. A thin (~150 μm) silicon or AlN chip containing a thin-film serpentine heater (5 × 5 mm) was bonded to the back of each sample. The entire sample assembly is housed in a sealed copper chamber with ports for a vacuum pump/gauge and a working fluid (water) inlet/outlet. A copper tube connected to a recirculating thermal bath is wrapped around the chamber multiple times to control the chamber temperature. The chamber is designed to create a controlled saturated liquid–vapor ambient (saturated water at 45 °C for the present work). Small (36 AWG) K-type thermocouple beads were bonded on eight different points along the centerline on the back sides of the substrates. The temperature of the thin-film heater was also directly monitored from its electrical resistance. Other details of the setup were reported in [9].

3.4. Results

The experimentally measured capillary performance parameters (K/R_{eff}) are compared with the predicted results in Fig. 6. The capillary performance parameter increases with the particle diameter, due in part to the reduced impact of the substrate on the viscous resistance. The improvement becomes modest, however, when the particle diameter is greater than approximately 60 μm. The experimental results are consistent with the predictions from our approximate model (the liquid fill factor = 0.5). The static contact angle of water on clean but slightly oxidized copper surfaces was approximately 30–50°.

As for heat transfer performance, the measured heat input versus wall superheat data from each sample (Fig. 7) are analyzed using 3D finite element simulations to account for heat spreading within the heater chip and the substrate. We iteratively search for an "average" heat transfer coefficient, which is assumed to be constant over the entire sample front surface, to match the experimental data. We call this the "effective heat transfer coefficient" in this report because the local heat transfer coefficient is not constant. The local heat transfer coefficient is expected to vary spatially over the sample surface as the local meniscus shapes adjust in response to heating to provide necessary capillary pumping power. Direct experimental confirmation of spatial variations in the meniscus curvature was reported in [17].

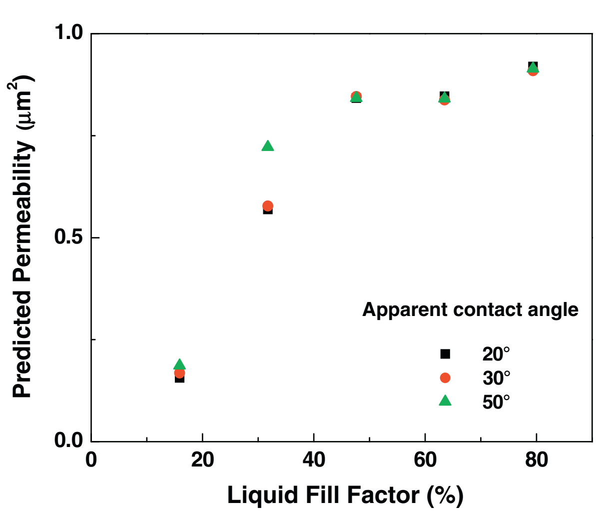

Fig. 5. Predicted liquid permeability of a monolayer powder sample as a function of the liquid fill factor for different values of the apparent contact angle.

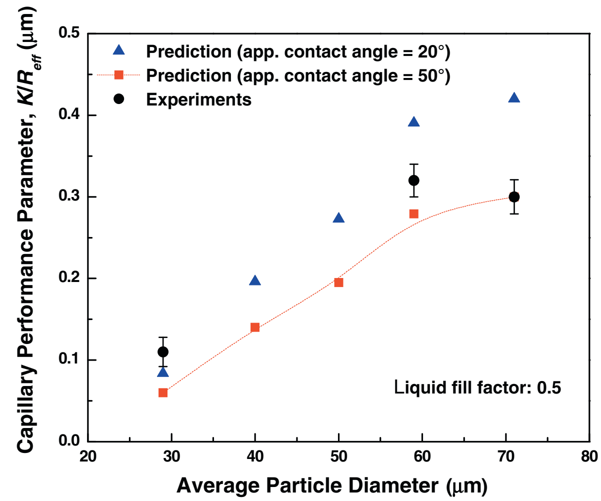

Fig. 6. Predicted and experimentally measured capillary performance of the Cu monolayer samples of different average powder diameters.

The experimentally determined effective heat transfer coefficients are approximately 5.5 W/cm^2 K for all the samples at heat fluxes approximately <15 W/cm^2 K. The values predicted from the static meniscus models for apparent contact angles 30–50° range from 5.9 to 6.4 W/cm^2 K, consistent with our experimental data. Appreciable changes in the heat transfer coefficient occur at heat fluxes as low as ~15 W/cm^2 for the sample with the smallest particles and ~50 W/cm^2 for the samples with bigger particles. One must take into account local dry out, bubble nucleation, and other phase change and flow phenomena to model the heat transfer coefficient at these higher heat fluxes.

4. Heat transfer performance of hybrid wicks

Our modeling and characterization study discussed above show that there exists an optimal range of particle diameter that maximizes the capillary performance of monolayers of sintered Cu particles. We therefore prepared hybrid wicks using liquid spreading layers made of Cu particles of target mean diameters of 60 μm for further characterization.

The heat transfer performance of the three different types of hybrid wicks was characterized using the experimental configuration illustrated in Fig. 8. Each evaporator wick was sintered on a 1 mm × 7 × 12 cm copper plate, which was then brazed onto a second copper plate via a 2.5 mm-thick copper spacer to achieve hermetic sealing.

For the wick with vertical columnar arteries, meshed copper screens were bonded to the condenser surface to feed the liquid to the arteries. For the wick with either converging lateral arteries or bi-porous structures, no separate condenser wick was used. Instead, a condensate pooled at the bottom of the vapor chambers by gravity is returned to the evaporator via the liquid supply structures.

Copper particles of nominal diameters 60 ± 5 μm were used to form the lateral arteries and bi-porous structures. Larger (D = 150 μm) particles were used to form the vertical columnar arteries. The vertical columnar arteries were 1.5 mm in height and 2.2 mm in diameter. The pitch was 3.52 mm. Each lateral artery is 1.5 mm thick and 1 mm wide.

A copper heating block incorporating cartridge heaters was used to apply heating over an area of 1 cm^2. A thermocouple was inserted into a pedestal directly machined onto the left copper plate to determine the heated wall temperature. For heat removal, aluminum water cooled blocks were fastened to the condenser side

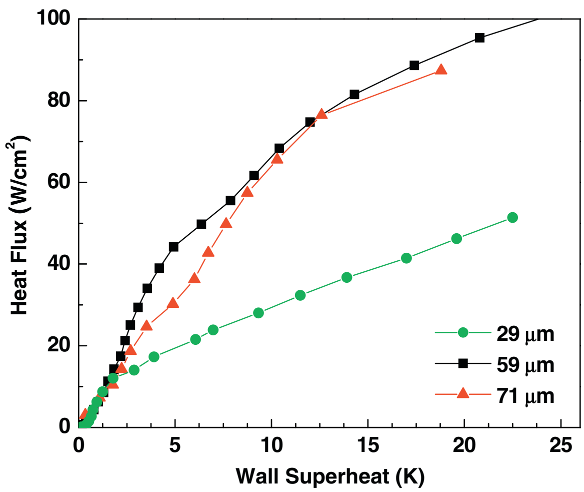

Fig. 7. Experimentally determined heat transfer performance of the Cu monolayer samples.

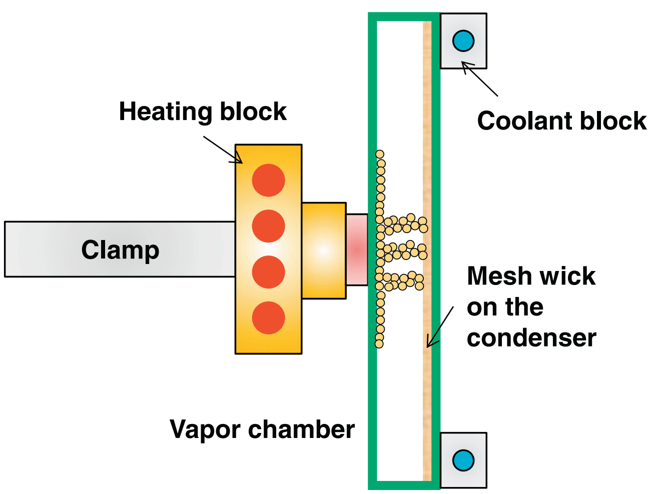

Fig. 8. Experimental configuration used to characterize the heat transfer performance of the hybrid wicks. The one with vertical columnar arteries is shown here. No separate mesh wick was used for the hybrid wicks with lateral converging arteries or bi-porous liquid supply structures.

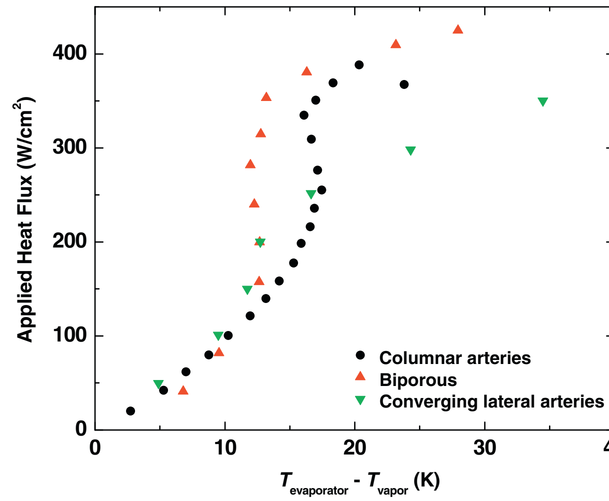

Fig. 9. Measured heat transfer performance of the hybrid wicks with three different liquid supply structures.

of the vapor chamber with graphite-foil based thermal interfaces. The cooling water flow rate was adjusted to allow for a nearly constant coolant temperature of 40 °C across the condenser. The condenser temperature was measured at six different locations.

Fig. 9 shows the measured heat flux versus superheat relations of the three wick designs. At heat flux values below 150 W/cm^2, the three designs show virtually identical performance, confirming that heat transfer is dominated by evaporation from the liquid spreading layers and is not strongly influenced by the type of liquid supply structures used. The measured data do deviate from each other at higher heat fluxes where the performance of liquid supply structures plays an increasingly important role.

Local dry-outs appear earlier for the wick with converging lateral arteries than the other two wicks. By increasing the number of lateral arteries and by making each artery narrower but thicker, one can theoretically improve the liquid feed performance without decreasing the exposed portion of the liquid spreading layer and thereby degrading the effective heat transfer coefficients. This is partly demonstrated in a set of follow-up experiments where the design with twice the number of arteries was shown to outperform the original design (Fig. 10). Having a larger fraction of the heated area covered by arteries still leads to reduced evaporation areas for the liquid spreading layer and hence degraded heat transfer performance at low heat fluxes. The performance improves at high heat fluxes and becomes comparable to the other two types of hybrid wicks when the liquid supply capability is a dominant limiting factor.

One interesting feature observed in all the wick designs is that, when the superheat reached around 15 K, the heat flux increases up to 350 W/cm^2 with minimal further changes in the evaporator superheat. This translates into improved heat transfer performance over this region. A similar behavior was observed in our previous experiments on samples that contained only liquid spreading layers (and no liquid supply structures).

The improved heat transfer performance may be a result in part of receding liquid menisci around Cu spheres toward the evaporator surface and hence decreasing average liquid layer thickness with increasing heat flux. High-speed imaging showed localized bubble nucleation and associated violent ejection of liquid droplets at comparable superheat values. These additional energy transport mechanisms may also partly explain this improved performance.

5. Prototype vapor chamber with low-CTE envelopes

We explore the use of aluminum nitride ceramic plates with direct bonded copper layers (DBC) as envelopes for our vapor chambers to reduce mismatch in CTE with semiconductor devices. Aluminum nitride has relatively high thermal conductivity and a CTE of approximately 4.5 ppm/°C.

The direct bonded copper layers are necessary for three reasons. First, copper is compatible with water, the most common and effective working fluid for microelectronics cooling. When in contact with water, Cu does not react and generate non-condensable gases or corrode. Copper/water heat pipes have been used successfully for decades, eliminating the need for extensive life testing that is required when new material/fluid combinations are proposed. Secondly, the copper layers allow for the use of conventional wick sintering and envelope sealing techniques. Thirdly, the copper layers on the external surfaces of the vapor chamber can be etched to form electric circuits.

Manufacturing of our low-CTE vapor chambers starts by sintering hybrid wick structures directly onto one of the copper layers on an envelope. A thin ring of copper-plated Kovar, also a low CTE material (5.9 ppm/°C), was used to space two envelopes apart and create a well-defined vapor space above the wick. A small-

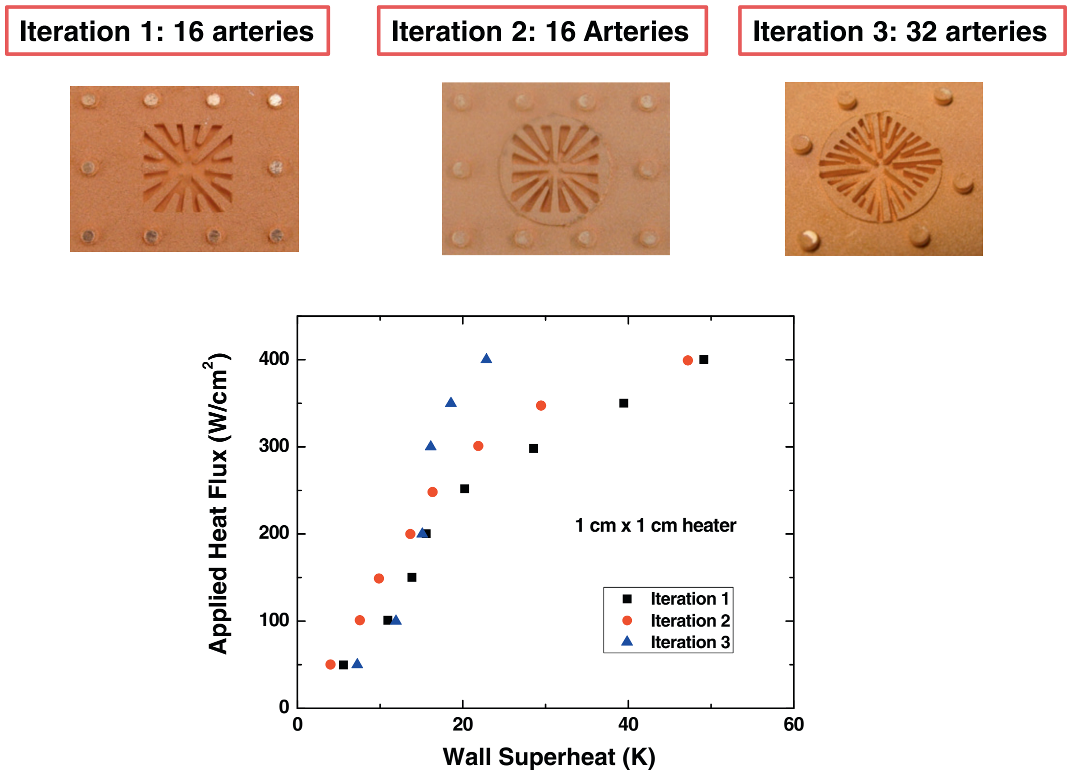

Fig. 10. Comparison of the heat transfer performance of hybrid evaporator wicks incorporating three different designs of the lateral converging arteries.

diameter fill tube was brazed into the Kovar ring to allow for evacuation and fluid charging. Brazing materials with proven compatibility with water (silver, copper, phosphorous alloys) were used to join the envelopes to the Kovar ring, forming the hermetic leak-tight vapor chamber. The brazing temperatures (640–815 °C) are well above the soldering temperatures (280–325 °C) typically used to attach electronic or optoelectronic devices. The assembled vapor chambers will therefore not be affected by subsequent chip attachment processes.

For reliable operations, one must ensure adequate hemeticity (e.g., less than 0.1% fluid loss per year) of vapor chambers. We used a helium mass spectrometer to measure a leak rate <9×10^{-10} Std. cc/sec, which may be translated into a fluid loss of 0.00005%/year for an 8 g fluid charge or >10 years of operation with negligible fluid leak. For more direct leak tests, several sealed vapor chambers were placed on burn-in stations maintained at 100 °C and weighed periodically to check for mass loss. Through these tests, we observed a weight loss <0.02% over a period of 9744 h.

Fig. 11 shows a 10×10 cm prototype specifically designed for potential application in the thermal management of high-power vertical cavity surface emitting laser (VCSEL) arrays. The top Cu layer of the vapor chamber is etched, gold/solder plated for direct attachment of VCSEL chips. Microchannel coolers are currently used for this application but they are susceptible to various failure mechanisms. Our vapor chambers enable efficient heat spreading, which in turn allows for the use of conventional low-fluid-velocity cold plates as heat sinks. This eliminates the need for costly high-pressure pumps and fluid conditioning equipment associated with microchannel coolers.

A hybrid wick specifically designed to accommodate an array of four 1×1 cm VCSEL chips is also shown in Fig. 11. Bi-porous liquid supply structures present challenges for thin and long planar vapor chambers due to the increased need for dedicated vapor space (to counter large vapor pressure drop) and less flexibility in designing and manufacturing the wicks around an array of distributed heaters. Vertical columnar arrays present challenges in achieving mechanical robustness and providing reliable contacts with condenser wicks. Based on these considerations, we select the refined converging lateral arteries as the liquid supply structures.

A typical set of test data from the prototype vapor chambers with four separate heater sections is shown in Fig. 12. The vapor chamber evaporator resistance is calculated from the temperature difference between a thermocouple inserted in a well drilled into the heat input pedestal and a thermocouple inserted into a well that protrudes into the vapor space and the electrical power input per square centimeter of the heat input area.

As seen in the plot, the evaporator thermal resistance decreases as the heat flux increases from 0 to approximately 350 W/cm^2,

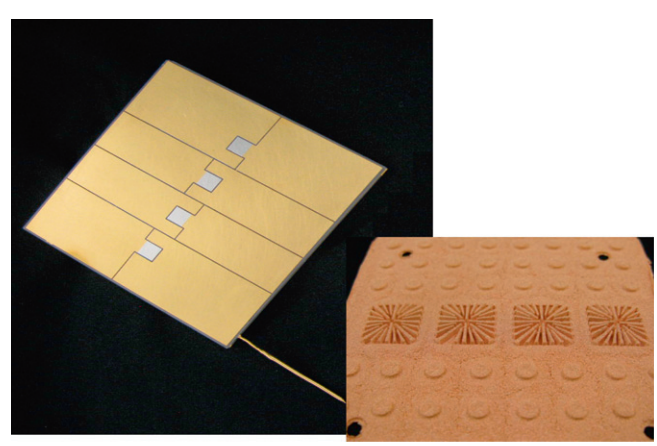

Fig. 11. Vapor chamber with etched electrical circuitry and plated gold/gold-tin solder layers for direct attachment of chips. Also shown is an optical image of the hybrid evaporator wick with laterally converging liquid supply structures specifically designed to accommodate 4 VCSELs.

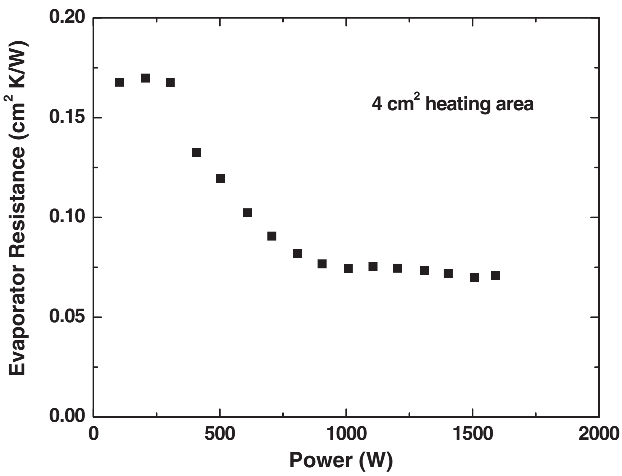

Fig. 12. Evaporator thermal resistance measured from a prototype vapor chamber with a hybrid wick with laterally converging arteries as a function of heat input power (four 1 cm × cm heaters).

consistent with the independent tests on the evaporator wicks discussed in Section 4. Above 400 W/cm^2, the wick structure begins to dry out and the thermal resistance increases until it reaches a critical limiting heat flux of approximately 550 W/cm^2. A total power through the vapor chambers of >1500 W was demonstrated with a heat input size of 4 cm^2. The evaporator thermal resistance as low as 0.075 °C/W/cm^2 was achieved. Prototypes incorporating hybrid wicks with vertical columnar arteries showed comparable performance.

6. Summary and conclusion

We presented our efforts in developing an innovative vapor chamber concept incorporating hybrid wicks of two integrated structures: a low thermal resistance spreading layer and a dedicated liquid supply structure. The spreading layer is comprised of a monolayer of sintered Cu particles to minimize the thermal resistance in the evaporator. Three different liquid supply structures were studied: vertical columnar arteries, converging lateral arteries, and bi-porous structures. All three designs were demonstrated to be able to handle heat fluxes >350 W/cm^2 over heating areas of 1 cm^2. A detailed modeling and experimental study of the capillary and heat transfer performance of monolayer liquid spreading layers was conducted to identify a range of optimal particle diameters. Hybrid wicks incorporating the three different liquid supply structures show virtually identical performance, confirming that heat transfer is dominated by evaporation from the liquid spreading layers.

We further established effective vapor chamber solutions for advanced chip layouts using low-CTE envelope materials. These envelope materials should allow the use of high thermal conductivity solders for direct attachments of semiconductor devices, further reducing overall thermal resistance. The work presented here can be utilized to develop high performance cooling solutions for high-power and high-power-density electronic components.

Acknowledgment

This work was supported in part by the Defense Advanced Research Project Agency (DARPA) and the Space and Naval Warfare Systems Center (SPAWARSYSCEN), San Diego, CA under Contract No. N66001-08-C-2007 (Program manager: Dr. Avi Bar-Cohen). The findings contained in this article are those of the authors and should not be interpreted as representing the official views or policies, either expressed or implied, of the DARPA or the Department of Defense (DoD).

References

[1] C. Ding, G. Soni, P. Bozorgi, B.D. Piorek, C.D. Meinhart, N.C. MacDonald, A flat heat pipe architecture based on nanostructured Titania, J. Microelectromech. Syst. 19 (2010) 878–884.
[2] H.P.J. de Bock, S. Chauhan, P. Chamarthy, S.E. Weaver, T. Deng, F.M. Gerner, et al., On the charging and thermal characterization of a micro/nano structured thermal ground plane, in: 2010 12th IEEE Intersociety Conference on Thermal and Thermomechanical Phenomena in Electronic Systems (ITherm), 2010, pp. 1–6.
[3] Q. Cai, C.-L. Chen, Design and test of carbon nanotube biwick structure for high-heat-flux phase change heat transfer, J. Heat Transfer 132 (2010) 052403.
[4] J.A. Weibel, S.V. Garimella, J.Y. Murthy, D.H. Altman, Design of integrated nanostructured wicks for high-performance vapor chambers, IEEE Trans. Compon. Packag. Manuf. Technol. 1 (2011) 859–867.
[5] G.S. Hwang, Y. Nam, E. Fleming, P. Dussinger, Y.S. Ju, M. Kaviany, Multi-artery heat pipe spreader: experiment, Int. J. Heat Mass Transfer 53 (2010) 2662–2669.
[6] G.S. Hwang, E. Fleming, B. Carne, S. Sharratt, Y. Nam, P. Dussinger, et al., Multi-artery heat-pipe spreader: lateral liquid supply, Int. J. Heat Mass Transfer 54 (2011) 2334–2340.
[7] T. Semenic, I. Catton, Experimental study of biporous wicks for high heat flux applications, Int. J. Heat Mass Transfer 52 (2009) 5113–5121.
[8] Y. Nam, S. Sharratt, C. Byon, S.J. Kim, Y.S. Ju, Fabrication and characterization of the capillary performance of superhydrophilic Cu micropost arrays, J. Microelectromech. Syst. 19 (2010) 581–588.
[9] Y. Nam, S. Sharratt, G. Cha, Y.S. Ju, Characterization and modeling of the heat transfer performance of nanostructured Cu micropost wicks, J. Heat Transfer 133 (2011) 101502.
[10] M.A. Hanlon, H.B. Ma, Evaporation heat transfer in sintered porous media, J. Heat Transfer 125 (2003) 644.
[11] J.A. Weibel, S.V. Garimella, M.T. North, Characterization of evaporation and boiling from sintered powder wicks fed by capillary action, Int. J. Heat Mass Transfer 53 (2010) 4204–4215.
[12] C.P. Migliaccio, S.V. Garimella, Evaporative heat and mass transfer from the free surface of a liquid wicked into a bed of spheres, Int. J. Heat Mass Transfer 54 (2011) 3440–3447.
[13] S. Sharratt, C. Peng, Y.S. Ju, Micro-post evaporator wicks with improved phase change heat transfer performance, Int. J. Heat Mass Transfer 55 (2012) 6163–6169.
[14] R. Ranjan, J.Y. Murthy, S.V. Garimella, Analysis of the wicking and thin-film evaporation characteristics of microstructures, J. Heat Transfer 131 (2009) 101001.
[15] R. Ranjan, J.Y. Murthy, S.V. Garimella, A microscale model for thin-film evaporation in capillary wick structures, Int. J. Heat Mass Transfer 54 (2011) 169–179.
[16] Y.-Y. Lin, T. Semenic, I. Catton, thermophysical properties of biporous sintered copper, in: ASME, 2005, pp. 785–791.
[17] F. Lefèvre, R. Rullière, G. Pandraud, M. Lallemand, Prediction of the temperature field in flat plate heat pipes with micro-grooves – experimental validation, Int. J. Heat Mass Transfer 51 (2008) 4083–4094.